Article

Discovery Medicine 2026; 38(207): 1115–1130
https://doi.org/10.24976/Discov.Med.202638207.90

A CD40LG-Centered 6-Gene Risk Model for Survival Stratification and Immunotherapy Benefit Prediction in Ovarian Cancer

Yuan Gao[1,2,†], Mingxia Ye[3,†], Yawen Wu[1,2], Liang Wen[1], Li-An Li[3], Yuanguang Meng[1,2,*]

[1]Senior Department of Obstetrics and Gynecology, Chinese PLA General Hospital, 100700 Beijing, China
[2]Chinese PLA Medical School, 100853 Beijing, China
[3]Senior Department of Obstetrics and Gynecology, The First Affiliated Center of Chinese PLA General Hospital, 100700 Beijing, China
*Correspondence: mengyuanguang@301hospital.com.cn (Yuanguang Meng)
[†]These authors contributed equally.
Submitted: 9 January 2026 Revised: 28 January 2026 Accepted: 4 March 2026 Published: 20 April 2026

Background: Ovarian cancer (OV) is a heterogeneous gynecologic malignancy with limited and patient-specific responses to immunotherapy. This study aimed to develop and validate a *CD40LG*-centered 6-gene signature based on immune-modulatory genes (IMGs) for prognostic stratification and prediction of immunotherapy response in OV patients.
Methods: Transcriptomic data and corresponding clinical annotations for normal and malignant ovarian tissues were retrieved from The Cancer Genome Atlas (TCGA) and Genotype-Tissue Expression (GTEx) database, respectively. The IMG-based prognostic signature (IMPS) was generated by identifying and integrating differentially expressed IMGs using univariate Cox regression and least absolute shrinkage and selection operator (LASSO)-Cox analysis. Tumor microenvironment (TME) characteristics, survival outcomes, and immunotherapy responses were analyzed with CIBERSORT, ESTIMATE, and Tumor Immune Dysfunction and Exclusion (TIDE) algorithms, and major IMGs were verified by quantitative real-time PCR (qRT-PCR).
Results: The IMPS, including *CD40LG*, *HMGB3*, *IL27RA*, *TNFRSF8*, *BTLA*, and *HLA-DOB*, exhibited significant prognostic ability. Kaplan-Meier curves demonstrated a survival advantage in the low-risk group ($p < 0.0001$), which was successfully cross-validated using the International Cancer Genome Consortium (ICGC) dataset. The low-risk group exhibited an anti-tumor immune phenotype (increased M1 macrophage infiltration, enriched antigen-processing pathways, activated T-cell signaling), whereas the high-risk group had higher immune-evasion potential (TIDE: r = 0.206, $p < 0.0001$). Analysis of the IMvigor210 trial indicated that individuals within the low-risk category exhibited a more favorable response to PD-1/PD-L1 blockade therapy. *CD40LG* expression was downregulated in OV tissues and associated with sensitivity to immunotherapy.
Conclusions: The *CD40LG*-centered 6-gene IMPS enables precise stratification of OV patients according to clinical outcomes and immunotherapy responsiveness, serving as a promising tool for guiding personalized immunotherapy strategies.

Keywords: ovarian cancer; immune modulatory genes; prognostic signature; tumor microenvironment; precision immunotherapy; biomarker

Introduction

Globally, ovarian cancer (OV) remains the most lethal malignancy among gynecological tumors. For individuals identified with late-stage disease, the clinical outlook is especially grim, with the probability of surviving beyond five years falling below the 30% threshold [1–3]. Most patients experience disease recurrence due to the development of therapeutic resistance, even after initial responses to platinum-based chemotherapy and cytoreductive surgery, resulting in persistently poor long-term outcomes [4,5]. Immune checkpoint blockade (ICB) has transformed oncology by producing long-lasting effects in lung cancer, melanoma, and other immunogenic tumors [6]. In stark contrast, ICB monotherapy yields objective response rates of only 6–15% in OV [7], underscoring the urgent need to elucidate the molecular mechanisms underlying its resistance to immunotherapy. Mechanistically, OV tumors evade immune surveillance not solely through PD-L1 upregulation or T cell exhaustion [8,9], but via coordinated dysregulation of broader immune-modulatory networks—including impaired co-stimulation (e.g., *CD40/CD40LG*) and defective antigen presentation (e.g., *HLA-DOB*) [10,11].

While clinical development has prioritized inhibitors targeting canonical checkpoints (CTLA-4, PD-1/PD-L1) [12] or emerging targets (*LAG3*, *TIM3*, *TIGIT*) [13], and combination strategies incorporating *IDO1* inhibitors or co-stimulatory agonists are under active investigation [14,15], a critical gap persists. To date, no multi-gene prognostic signature has been established that leverages a broad set of immune-modulatory genes (IMGs) to stratify OV patients

by prognosis or ICB responsiveness. Notably, the IMGs analyzed in this study were curated from published studies of immune checkpoint-related biology, encompassing not only canonical checkpoint molecules but also their associated signaling ligands, receptors, and downstream effectors that regulate tumor microenvironment (TME) immune dynamics.

To bridge this gap, we systematically analyzed transcriptomic profiles of IMGs across OV cohorts to construct a novel IMGs-based prognostic signature (IMPS). Comprising six functionally diverse genes—including antigen-presentation regulator *HLA-DOB*, the co-stimulatory ligand *CD40LG*, and the danger-associated molecular pattern *HMGB3*, among others—the IMPS captures multidimensional immune dysregulation within the TME. Using the TCGA-OV and IMvigor210 cohorts, we show that the IMPS reliably stratifies patients into low- and high-risk groups with different TME characteristics (e.g., TCR activation and M1 macrophage infiltration), predicted ICB responses, and survival outcomes. The clinical relevance of key IMPS components was further confirmed experimentally using quantitative real-time PCR (qRT-PCR).

Collectively, our IMPS represents a biologically grounded and clinically actionable biomarker. It offers a framework to stratify OV patients and identify those most likely to benefit from immunotherapy — thereby advancing the goal of personalized immuno-oncology in this challenging malignancy.

Methods

Data Acquisition and Processing

Gene expression information from the TCGA-TARGET-GTEx dataset, including RNA-seq expected counts from 427 OV tissues and 88 normal ovarian tissues, was acquired for differential expression analysis in this study using the UCSC Xena platform (https://xenabrowser.net/datapages/, accessed on January 17, 2024) [16]. Additionally, the GDC Data Portal (https://portal.gdc.cancer.gov/, visited on January 17, 2024) was used to download clinical metadata and RNA-seq data (TPM format) for the TCGA-OV cohort. The original cohort's baseline clinical features (n = 400) are displayed in **Supplementary Table 1**. A final group of 390 patients was selected for further analysis after excluding patients with incomplete clinical data or an overall survival (OS) of less than 30 days. An independent cohort (OV-AU, n = 81) was acquired from the International Cancer Genome Consortium (ICGC, https://dcc.icgc.org, accessed on January 17, 2024) to serve as an external validation set and evaluate the generalizability of our risk model.

To develop our predictive model and conduct subsequent analyses, we identified a set of 373 IMGs, drawing upon established literature on molecules associated with immune checkpoints [17–21]. These IMGs encompass not only canonical immune checkpoint molecules (e.g., *BTLA*) and their associated ligands or receptors (e.g., *CD28*, *CD80/86*), but also non-canonical immune regulators that interact with checkpoint pathways (e.g., HLA-DOB) (**Supplementary Table 2**).

Identifying IMGs That Are Differentially Expressed

Differential gene expression across the two risk subgroups and between tumor and normal specimens was determined through the 'DESeq2' computational framework. Genes that satisfied the criteria of $|\log_2(\text{fold change})| > 1$ and adjusted p value (adj. p) < 0.05 were classified as differentially expressed genes (DEGs). Candidate differentially expressed IMGs (DE-IMGs) were chosen for further analysis after the distribution of DEGs was visualized using the "ggVolcano" R package (https://github.com/BioSenior/ggVolcano) , and overlapping genes between DEGs and IMGs were found using Venn diagrams.

Building and Verifying the Prognostic Model Based on IMGs

Using univariate Cox proportional hazards regression (R package: "survival"; https://cran.r-project.org/package=survival) with a significance threshold of $p < 0.05$, DE-IMGs associated with OS were initially found in the TCGA-OV cohort. In order to reduce multicollinearity and exclude redundant variables, candidate genes were then subjected to least absolute shrinkage and selection operator (LASSO) regression for feature selection and dimensionality reduction using R package "glmnet" (https://cran.r-project.org/package=glmnet) [22]. To identify the best prognostic signature and acquire regression coefficients for model construction, genes retained after LASSO regression were then incorporated into a multivariate Cox proportional hazards model. The following formula was used to establish each patient's individualized risk score:

$$\text{Risk score} = \sum_{i=1}^{n} (\beta_i \times \exp_i) \quad (1)$$

The regression coefficient of signature gene i is denoted by β_i, the expression level of gene i by exp_i, and the total number of signature genes is represented by n. Patients within the TCGA-OV training set were stratified into two risk subgroups based on the median risk value. To ascertain the prognostic accuracy of our signature across various intervals (1, 2, 3, and 5 years), time-dependent receiver operating characteristic (ROC) analysis was implemented via the 'timeROC' library (https://cran.r-project.org/package=timeROC). The predictive performance at each specific time point was quantified by calculating the area under the curve (AUC) values. To visually depict the risk stratification framework and its clinical implications, a multi-dimensional heatmap was generated using

the 'pheatmap' package (https://cran.r-project.org/package=pheatmap). This integrated visualization displays the gradient of risk scores alongside the expression profiles of signature genes and the longitudinal survival distribution of the TCGA-OV patients. The same analytical procedure was applied to an independent ICGC OV-AU cohort for external validation to assess the IMPS's performance and generalizability.

Functional Enrichment Profiling

Using the R package 'clusterProfiler' (Bioconductor, https://bioconductor.org/packages/clusterProfiler/), functional enrichment analyses were performed to identify Kyoto Encyclopedia of Genes and Genomes (KEGG) pathways and Gene Ontology (GO) terms associated with the screened gene sets [23]. The gene annotation data came from the "org.Hs.eg.db" database (Bioconductor, https://bioconductor.org/packages/org.Hs.eg.db/). Using the "enrichplot" package (Bioconductor, https://bioconductor.org/packages/enrichplot/), gene set enrichment analysis (GSEA) was performed on the MSigDB gene sets "c5.go.v7.0.symbols.gmt" and "c2.cp.kegg.v7.0.symbols.gmt" (MSigDB, https://www.gsea-msigdb.org/gsea/msigdb). Statistical significance was set at a false discovery rate (FDR) <0.05, with significant items and pathways reported using normalized enrichment scores (NES) and adjusted p values.

Nomogram Construction and Validation

Univariate Cox regression was employed to screen potential prognostic factors (e.g., age, tumor stage, risk score), retaining those with $p < 0.05$ for multivariable analysis. Significant predictors from the multivariable Cox regression ($p < 0.05$) were incorporated into a nomogram constructed with the "rms" package (https://cran.r-project.org/package=rms). Internal validation was performed by bootstrap resampling (1000 iterations). To evaluate the reliability of the nomogram, calibration curves were used to compare the predicted outcomes with the actual survival rates [24,25]. The discriminative efficiency was measured using the concordance index (C-index) alongside time-dependent ROC analysis (focusing on 1-, 3-, and 5-year intervals). Furthermore, decision curve analysis (DCA) was implemented to determine the clinical net benefit and practical utility of our integrated model.

Assessment of Mutational Load

To explore the potential link between genomic instability and immunotherapeutic efficacy, we obtained somatic mutation profiles for the TCGA-OV patients from the cBioPortal database (https://www.cbioportal.org/; accessed on January 17, 2024) [26,27]. Mutational profiles were analyzed and visualized using the 'maftools' package (Bioconductor, https://bioconductor.org/packages/maftools/). The cohort was stratified into high- and low- tumor mutation burden (TMB) groups, and integrated oncoplots were used to examine the distribution of mutation types and frequencies, aiming to uncover distinct patterns of genetic alterations between the two groups.

Tumor Immune Microenvironment Analysis

To quantify the infiltration levels of 22 distinct leukocyte subsets within the TCGA-OV samples, we utilized the CIBERSORT deconvolution method employing the LM22 signature via the 'IOBR' R framework (https://github.com/IOBR/IOBR) [28]. Only samples demonstrating statistical significance ($p < 0.05$) were retained for subsequent analysis. The ESTIMATE algorithm was concurrently applied to derive tumor purity, immune, and ESTIMATE scores [29,30]. We then analyzed the variations in TME composition between the high- and low-risk groups.

Prediction of Immunotherapy Response

To predict the association between our risk model and response to immune checkpoint blockade (ICB), we employed a dual approach. First, we applied the Tumor Immune Dysfunction and Exclusion (TIDE) algorithm (http://tide.dfci.harvard.edu/; accessed on January 17, 2024) to predict patient responses [31–33]. Second, we validated the model using the IMvigor210 cohort (obtained via the 'IMvigor210CoreBiologies' package; http://research-pub.gene.com/IMvigor210CoreBiologies/), which contains clinical and genomic data from 298 individuals with metastatic urothelial carcinoma undergoing anti-PD-L1 treatment. In this validation set, subjects were categorized into distinct risk strata using a survival-derived optimal threshold of the risk score.

Patient Sample Collection, RNA Extraction, and qRT-PCR

Ethical approval for this study was obtained from the Ethics Committee of the Chinese PLA General Hospital (Approval No. of Ethics Committee: S2024-482-01), and all participants provided written informed consent. Between March and June 2024, 10 fresh epithelial ovarian cancer (EOC) tissues and 5 normal ovarian tissues (from patients with benign gynecological conditions) were collected. Inclusion criteria for the EOC group were: (1) histologically confirmed EOC; (2) no prior history of radiotherapy, chemotherapy, or immunotherapy; and (3) availability of complete clinical and follow-up data. Participants with severe organ dysfunction, acute infections, or those who declined consent were excluded.

Total RNA was isolated with TRIzol™ reagent (Invitrogen, Cat. No. 15596026; Waltham, MA, USA), followed by cDNA synthesis using HiScript III RT SuperMix (Vazyme, Cat. No. R323-01; Nanjing, China). RNA levels were quantified using quantitative real-time PCR (qRT-PCR) with SupRealQ Purple Universal SYBR qPCR

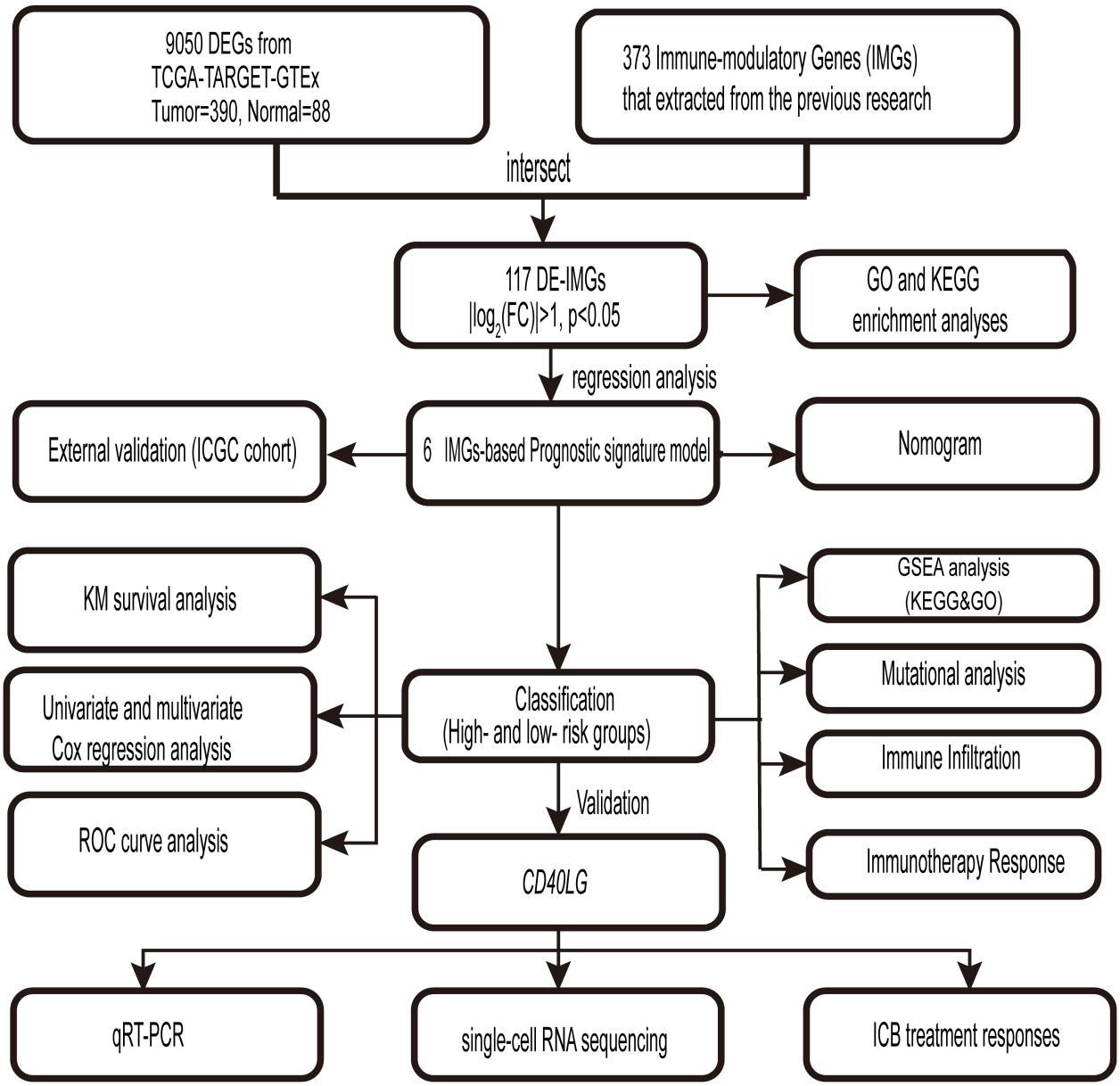

Fig. 1. Flowchart of the study.

Master Mix (Vazyme, No. Q711-02/03; Nanjing, China), and expression was normalized to *GAPDH*. The primer sequences used are provided in **Supplementary Table 3**. Each sample was assayed in triplicate, and relative expression was determined via the $2^{-\Delta\Delta CT}$ method.

Statistical Analysis

The statistical analyses were performed using R (v4.3.2, https://www.r-project.org/; R Foundation for Statistical Computing, Vienna, Austria) and GraphPad Prism (v10.1, GraphPad Software, San Diego, CA, USA). The Shapiro-Wilk test was used to verify the normality of continuous variables. Variables that passed the normality test ($p > 0.05$) were analyzed using the independent-samples *t*-test, while those that did not were analyzed using the Wilcoxon rank-sum test. Spearman's rank correlation was used to evaluate relationships between continuous variables. The Chi-squared test or Fisher's exact test was used to compare categorical variables, as applicable. A two-sided *p*-value less than 0.05 was considered statistically significant. Fig. 1 shows a schematic overview of the study design.

Results

Identification of DE-IMGs in OV and Functional Enrichment Analysis

Comparison of OV samples with normal ovarian tissues identified 9050 DEGs, comprising 4920 upregulated and 4130 downregulated genes (Fig. 2A, **Supplementary**

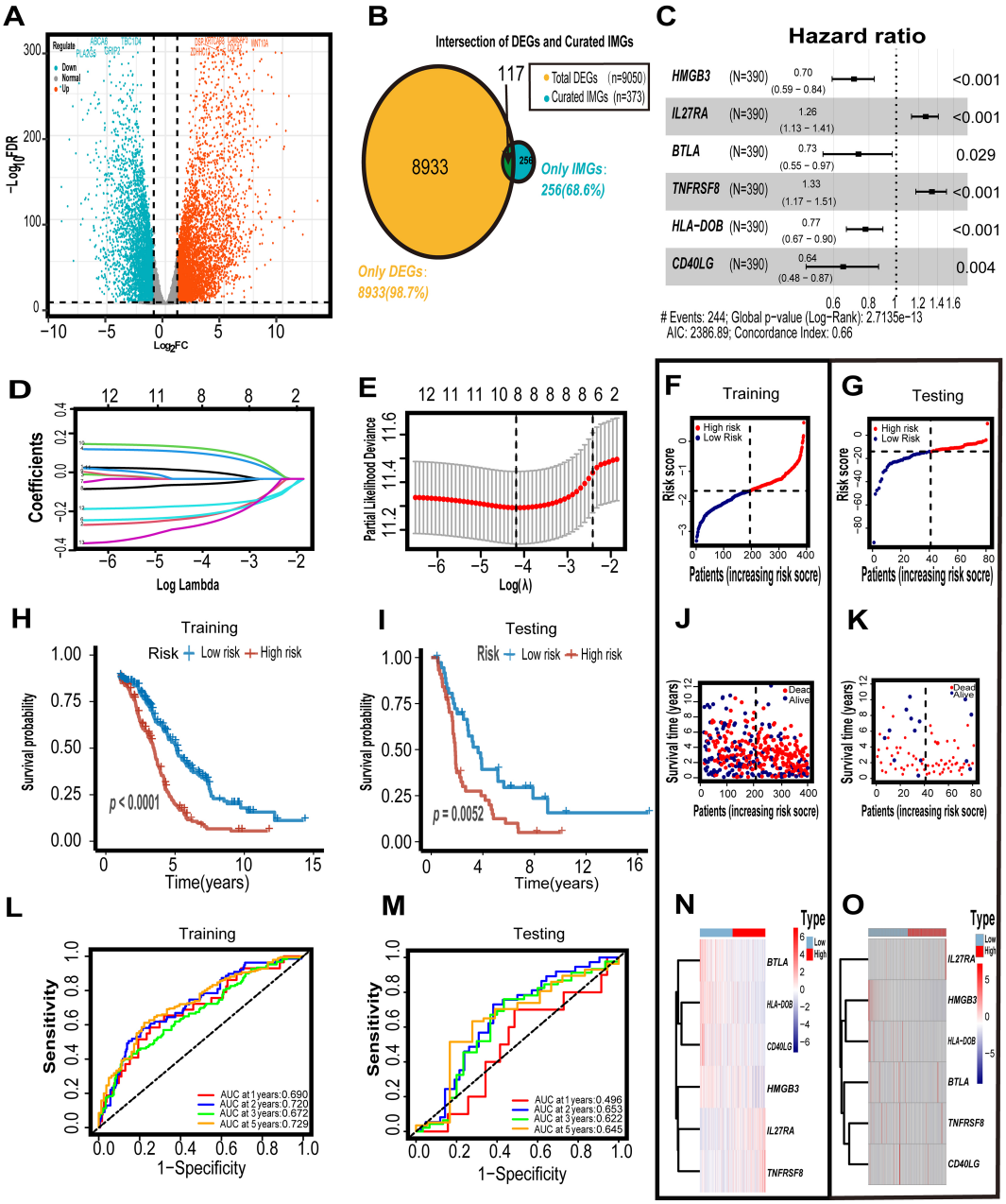

Fig. 2. Development and assessment of a prognostic signature. (A) Volcano plot depicting the 9050 DEGs between OV and normal tissues. (B) Venn diagram illustrating the intersection of 9050 DEGs and 373 curated IMGs, yielding 117 DE-IMGs (1.3% of total DEGs and 31.4% of curated IMGs). (C) Forest plot of the six prognostic genes with their hazard ratios (HRs) from multivariate Cox regression. (D) Coefficient profiles of candidate genes derived from LASSO regression. (E) The ideal λ value based on partial likelihood deviance using 10-fold cross-validation. (F,J,N) Tripartite analysis of the TCGA training set: risk scores, survival status, and signature gene expression. High-risk patients (right side) exhibit shorter survival times and higher mortality rates compared to low-risk patients (left side). (G,K,O) Corresponding plots for the independent ICGC validation cohort, showing consistent risk stratification and gene expression patterns. (H,I) Significant survival disparity between risk groups is shown by KM analysis in both TCGA (H) and ICGC (I) datasets. (L,M) Time-dependent ROC analysis for 1-, 2-, 3-, and 5-year survival in TCGA (L) and ICGC (M) cohorts. DEGs, differentially expressed genes; IMGs, immune-modulatory genes; DE-IMGs, differentially expressed IMGs; LASSO, least absolute shrinkage and selection operator; TCGA, The Cancer Genome Atlas; ICGC, International Cancer Genome Consortium; KM, Kaplan-Meier; ROC, receiver operating characteristic.

Table 4). Intersecting these DEGs with the curated set of 373 IMGs yielded 117 DE-IMGs (Fig. 2B, **Supplementary Table 5**).

To systematically characterize the functional landscape of these DE-IMGs, we performed GO and KEGG enrichment analyses. GO biological process (BP) analysis revealed significant enrichment in immune-related processes, including the regulation of T cell activation, immune cell adhesion, and lymphocyte proliferation. Molecular function (MF) analysis showed enrichment for terms primarily related to antigen binding and immune receptor activity. According to the cellular component (CC) analysis, there was a significant concentration of genes within MHC class II protein complexes, alongside various structures related to antigen presentation (**Supplementary Fig. 1A**, **Supplementary Table 6**). KEGG pathway analysis revealed strong enrichment of key immunoregulatory pathways, such as the T cell receptor signaling pathway, the PD-1/PD-L1 checkpoint pathway, and the antigen processing and presentation pathway (**Supplementary Fig. 1B**, **Supplementary Table 7**).

Construction and Validation of the CD40LG-Centered 6-Gene Prognostic Signature

We constructed a 6-gene IMPS based on DE-IMGs. Out of the 117 potential DE-IMGs, 13 survival-associated genes were found using univariate Cox regression analysis ($p < 0.05$; **Supplementary Fig. 2**). The feature genes were further refined to 8 ideal candidates through subsequent LASSO regression with 10-fold cross-validation. A partial likelihood deviance plot was used to determine the ideal λ value (Fig. 2D,E). Multivariate Cox regression analysis ultimately retained 6 prognostic genes (*HMGB3*, *IL27RA*, *BTLA*, *TNFRSF8*, *HLA-DOB*, and *CD40LG*), with their corresponding hazard ratios (HRs) presented in a forest plot (Fig. 2C). The following formula was used to determine the risk score:

$$\begin{aligned}\text{risk score} = {} & (-0.352 \times \text{ expression of } \textit{HMGB3}) \\ & + (0.234 \times \text{expression of } \textit{IL27RA}) \\ & + (-0.316 \times \text{expression of } \textit{BTLA}) \\ & + (0.285 \times \text{expression of } \textit{TNFRSF8}) \\ & + (-0.258 \times \text{expression of } \textit{HLA-DOB}) \\ & + (-0.441 \times \text{expression of } \textit{CD40LG})\end{aligned} \quad (2)$$

To evaluate the model's predictive performance, the TCGA-OV training set (n = 390) was divided into high- and low-risk groups based on the median risk score. Kaplan-Meier curves indicated that individuals in the high-risk group experienced significantly poorer survival outcomes compared to their low-risk counterparts ($p < 0.0001$; Fig. 2H). Furthermore, time-dependent ROC analysis yielded AUC values of 0.690, 0.720, 0.672, and 0.729 at the 1-, 2-, 3-, and 5-year intervals, respectively, confirming the signature's stable predictive performance (Fig. 2L). Detailed survival data are provided in **Supplementary Table 8**. Risk score distribution and survival status analyses provided additional evidence: increased risk scores were associated with shorter survival times and an increased incidence of death events. These results together confirm the model's ability to stratify patients effectively (Fig. 2F,J,N).

The predictive model underwent further verification in a distinct ICGC cohort, reinforcing its validity. Consistent with the training set, KM analysis using the identical risk threshold showed significantly worse outcomes for the high-risk group ($p = 0.0052$; Fig. 2I). The model's predictive accuracy, as evaluated by time-dependent ROC curves, improved for longer-term forecasts, with AUCs of 0.653, 0.622, and 0.645 for 2, 3, and 5 years, respectively, compared to 0.496 at 1 year (Fig. 2M). Visual inspection of survival status scatterplots (Fig. 2G,K,O) corroborated these findings, showing a negative correlation between risk scores and survival duration. Combined with Kaplan-Meier survival curves (Fig. 2H,I) and time-dependent ROC curves (Fig. 2L,M), these results collectively confirm the model's robust ability to stratify patients for medium- to long-term prognostic.

Overall, the IMPS consistently and robustly stratified patient risk across independent cohorts.

Creating and Verifying an Independent Prognostic Nomogram

To determine the independent prognostic value of the IMPS model, univariate and multivariate Cox regression analyses were conducted with age, tumor stage, and risk score. As depicted in Fig. 3A, univariate Cox regression revealed a strong association between poor survival and both age ($p < 0.001$) and the calculated risk score ($p < 0.001$). Furthermore, the independent predictive value of age ($p = 0.005$) and the risk score ($p < 0.001$) was sustained in the multivariate model after adjusting for clinical covariates (Fig. 3B).

Time-dependent ROC analysis further showed that the risk score was more effective than age and tumor stage in predicting survival at 1-year (AUC = 0.682), 3-year (AUC = 0.671), and 5-year (AUC = 0.726) timepoints (Fig. 3C–E). A comprehensive prognostic nomogram was constructed by incorporating the risk score into clinical parameters, including age and tumor stage, to facilitate practical clinical utility (Fig. 3F). This integrated model increased prediction accuracy, with AUCs of 0.719, 0.714, and 0.731 at 1-, 3-, and 5-year timepoints, respectively. Both the nomogram and risk score had a C-index above 0.5 (Fig. 3G), supporting their statistically significant ability to discriminate OS in OV.

Calibration curves showed favorable agreement between the predicted and observed survival probabilities, with only slight deviations at the 3-year and 5-year timepoints (Fig. 3H)—confirming the model's validity for long-

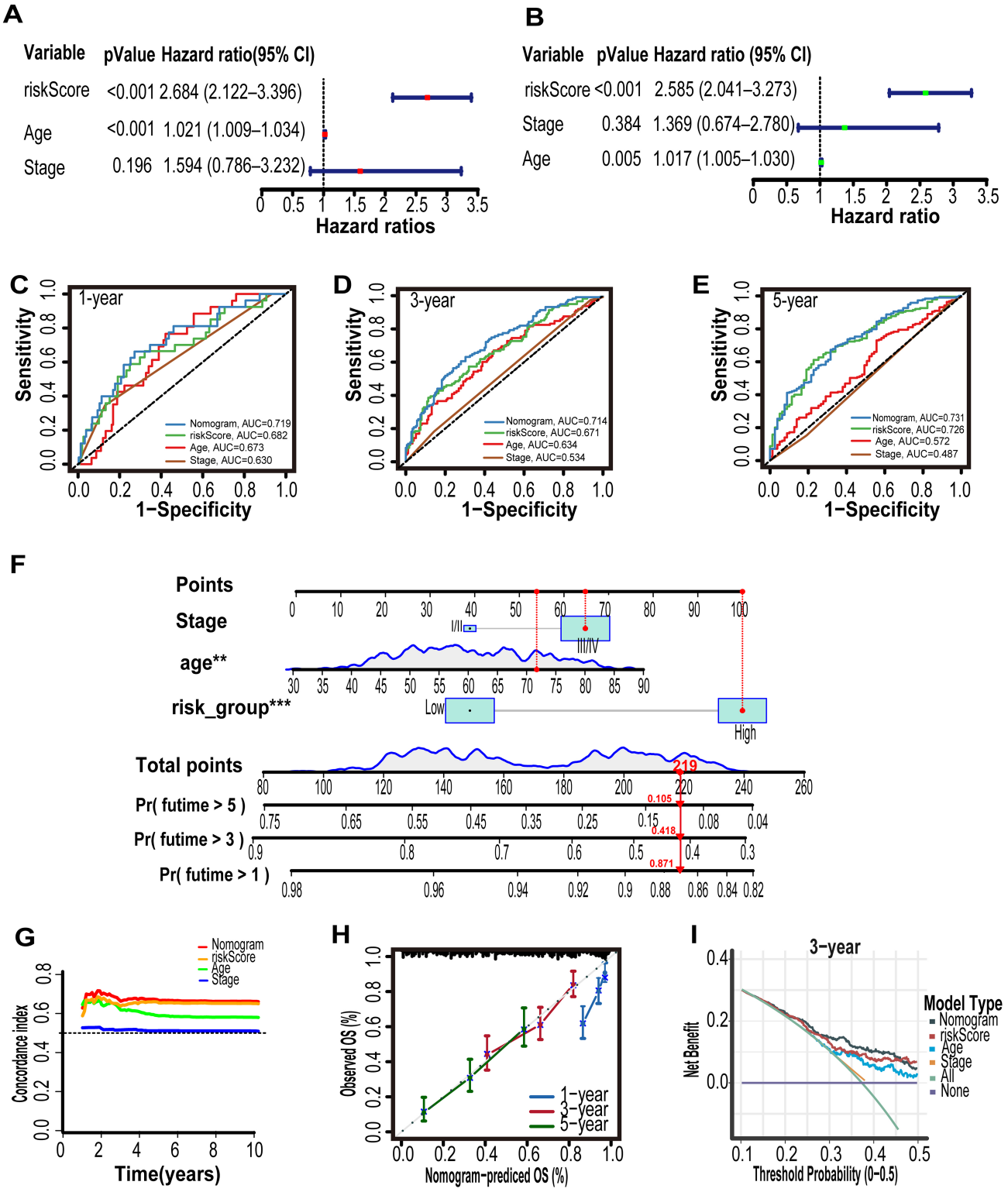

Fig. 3. Prognostic independence, predictive performance, and clinical utility of the IMPS and integrated nomogram in OV. Cox regression studies of the signature with clinical phenotypes, both univariate (A) and multi-variate (B). The nomogram, risk score, age, and stage prediction accuracy at 1-year (C), 3-year (D), and 5-year (E) timepoints were compared using time-dependent ROC curves. (F) Prognostic nomogram estimating individual 1-, 3-, and 5-year OS rate by combining age, stage, and risk score. (G) To evaluate the nomogram's and the other clinical features' identification and predicting abilities, a concordance index (C-index) was created. (H) Calibration plot analysis to evaluate nomogram accuracy. (I) The decision curve analysis plot. ** $p < 0.01$, *** $p < 0.001$. IMPS, IMG-based prognostic signature; OV, ovarian cancer; OS, overall survival.

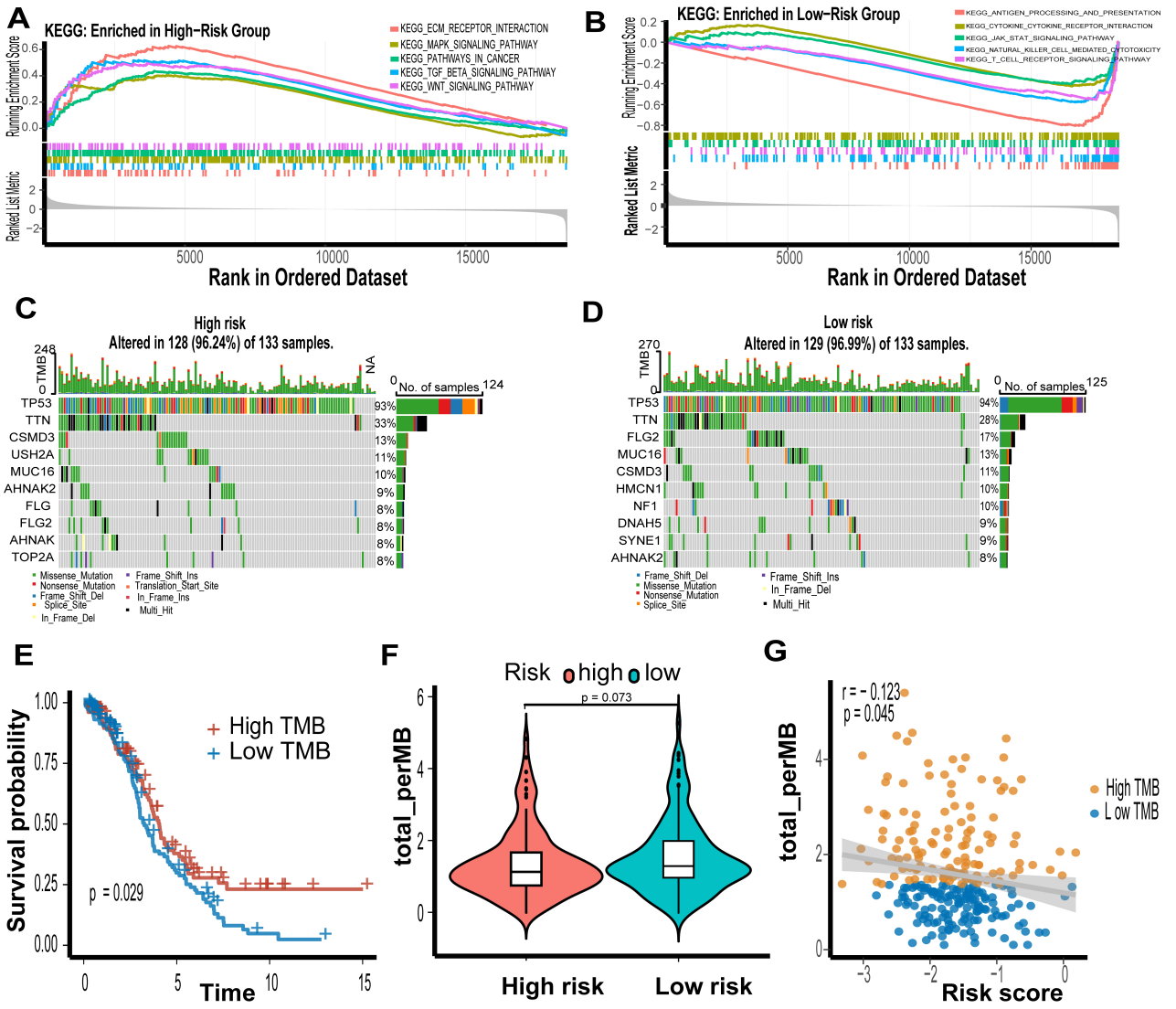

Fig. 4. Functional enrichment, mutational landscape, and prognostic impact of TMB across risk groups. GSEA was performed on DEGs between the high-risk (A) and low-risk (B) groups; Somatic mutation profiles in the high-risk (C) and low-risk (D) groups are depicted via waterfall plots. (E) KM survival analysis stratified by median TMB. (F) Comparison of TMB values between the high- and low-risk groups. (G) Spearman correlation between risk score and TMB. TMB, tumor mutation burden; GSEA, gene set enrichment analysis.

term risk assessment. The DCA demonstrated that both the risk score and nomogram yielded greater net clinical benefit than "treat-all" or "treat-none" strategies across a broad range of threshold probabilities (Fig. 3I). Together, these results underscore the prognostic significance of the IMPS and highlight the additional value of integrating clinical variables into the nomogram.

Functional Enrichment and Mutation Landscape in Different Risk Groups

Different biological aspects were shown in GSEA of DEGs between high- and low-risk groups (**Supplementary Table 9**). A TME marked by ECM remodeling and pro-oncogenic signaling activation was indicated by significant enrichment in KEGG pathways linked to extracellular matrix (ECM)–receptor interaction, MAPK signaling, cancer pathways, TGF-β signaling, and Wnt signaling in the high-risk group (Fig. 4A). On the other hand, as shown in Fig. 4B, the low-risk group showed increased adaptive and anti-tumor immunity through enrichment in antigen processing and presentation, cytokine–cytokine receptor interaction, JAK-STAT signaling, NK cell–mediated cytotoxicity, and T cell receptor signaling. These findings were supported by GO biological process analysis, showing that immune-related pathways like T cell activation and cytokine generation predominated in the low-risk cohort, while the high-risk patients were primarily characterized by angiogenesis and extracellular matrix arrangement (**Supplementary Fig. 3A,B**).

Next, we assessed TMB, a widely-recognized biological indicator for prognosis and response to immunotherapy [34]. Differences in the mutational landscape were observed between the risk groups, with somatic mutation analysis indicating comparable mutation frequencies between the two groups (96.99% in the low-risk group vs. 96.24% in the high-risk group) (Fig. 4C,D). TP53 mutations were highly prevalent across both groups (94% in the low-risk group vs. 93% in the high-risk group), reflecting their foundational role in the pathogenesis of ovarian cancer—particularly high-grade serous ovarian cancer (HGSOC). TTN mutations showed a slight enrichment in the high-risk group (33% vs. 28%), though these differences were minimal and not over-interpreted. Spearman correlation analysis identified a statistically significant but weak negative correlation between TMB and risk score (r = –0.123, $p = 0.045$; Fig. 4G). KM analysis stratified by the median TMB revealed that patients with high TMB had significantly longer overall survival ($p = 0.029$; Fig. 4E). Although the TMB itself did not differ significantly between the risk groups ($p = 0.073$; Fig. 4F), this result supports the prognostic value of TMB in our cohort.

Characterization of Tumor Immune Microenvironment Differences Between High- and Low-Risk Groups

The TME, a critical regulatory hub governing cancer progression and therapeutic response, exhibits distinct immunological features, with the composition and functional state of immune cells directly influencing tumor immune surveillance efficacy and treatment outcomes [35]. Using the CIBERSORT algorithm, we systematically profiled immune cell infiltration across risk subgroups and identified significant associations between risk classification and immune phenotypes. The low-risk group had an immunologically active phenotype, as shown in Fig. 5A. This was evidenced by a notable enrichment of M1 macrophages ($p < 0.001$), follicular helper T cells ($p < 0.05$), activated memory $CD4^+$ T cells ($p < 0.01$), and $\gamma\delta$ T cells ($p < 0.05$), all of which suggested enhanced anti-tumor immunity. A hierarchical clustering heatmap further corroborated these distinct immune patterns (**Supplementary Fig. 4A,B**), supporting the marked association between risk groups and immune landscape.

We used the ESTIMATE technique to measure tumor purity, immunological score, and ESTIMATE score across risk groups, providing a comprehensive characterization of the TME. A significant elevation in immune scores was observed within the low-risk group compared to the high-risk counterpart ($p < 0.01$; Fig. 5F), suggesting a more immune-infiltrated microenvironment. However, no discernible difference in tumor purity or ESTIMATE scores was observed across the groups (Fig. 5G,H). Spearman correlation analysis showed statistically significant but weak negative correlations between risk scores and immune scores (r = –0.178, $p = 0.00041$) as well as ESTIMATE scores (r = –0.100, $p = 0.04949$) (Fig. 5B,C). A weak and marginally significant correlation was also observed between tumor purity and risk score (Fig. 5D). Together, these results imply that the risk signature primarily captures immune infiltration status rather than tumor cellularity.

Association Between Prognostic Signature and Immunotherapy Response

To investigate whether our IMPS reflects tumor immune escape mechanisms and thus predicts ICI outcomes, we first performed TIDE analysis in the TCGA-OV cohort, then validated the signature's clinical utility in the IMvigor210 cohort. Detailed data are presented in **Supplementary Tables 10,11**. According to TIDE analysis, the immune evasion scores in the high-risk group were considerably greater than those of the low-risk group ($p < 0.001$; Fig. 5J,K). This finding is in line with the established correlation between lower ICI responsiveness and higher TIDE scores [31]. A substantial positive connection between risk scores and TIDE scores was also validated by Spearman correlation analysis (r = 0.206, $p < 0.0001$; Fig. 5L), highlighting the intimate relationship between the risk signature and an immunosuppressive TME that facilitates immune escape.

We further validated the risk signature in the IMvigor210 cohort. Using maximally selected rank statistics, an optimal risk score cutoff of –1.59 was determined, stratifying patients into high-risk (n = 149) and low-risk (n = 149) groups, with the stratification result visualized in **Supplementary Fig. 4C**. KM survival curves validated the clinical utility of our model within the ICI-treated population, demonstrating that individuals in the high-risk group experienced significantly diminished overall survival compared to those at low risk ($p < 0.0001$; Fig. 5E). Notably, patients with complete or partial remission (CR/PR) had significantly lower risk ratings than patients with stable or progressive illness (SD/PD) ($p = 0.016$; Fig. 5I). These results collectively establish the low-risk signature as a promising biomarker for identifying patients likely to benefit from anti-PD-L1 therapy, providing a rationale for patient stratification in clinical practice.

Prognostic and Immunotherapeutic Relevance of CD40LG in Ovarian Cancer

Among the 6 genes in the IMPS, *CD40LG* exhibited the most prominent prognostic weight, with the largest absolute regression coefficient ($\beta = –0.441$) in the multivariate Cox regression model. This negative coefficient indicated that lower *CD40LG* expression was associated with higher prognostic risk, highlighting its dominant contribution to the signature's survival predictive capacity. Given that the functional role of *CD40LG* in OV remains underexplored, we further performed experimental validation to elucidate its clinical and biological significance.

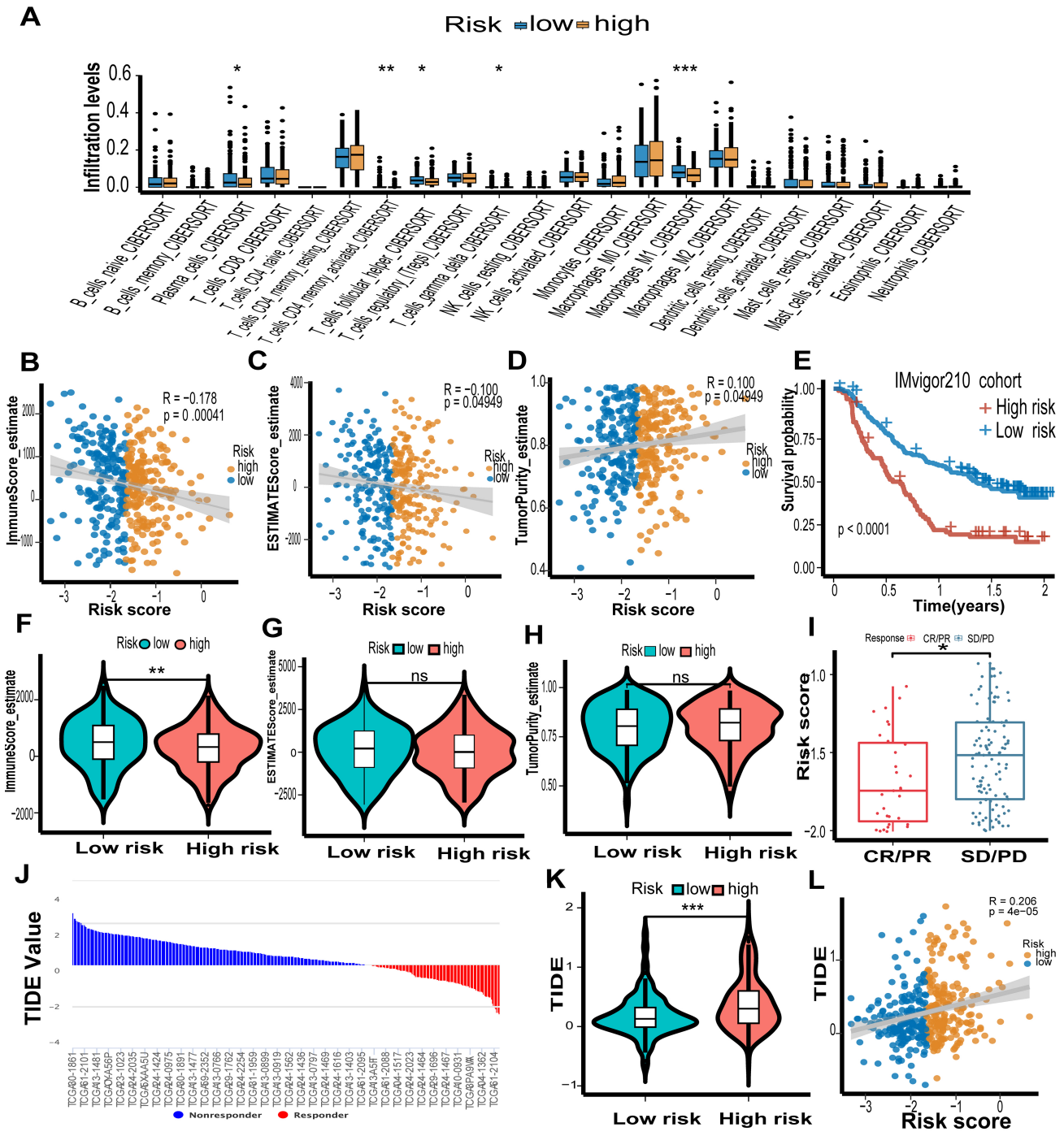

Fig. 5. Immune microenvironment profiling and immunotherapy response prediction. (A) Relative abundance of immune cell populations inferred by CIBERSORT. (B–D) Association between the prognostic risk score and key immune indicators, including immune cell enrichment (B), ESTIMATE-derived immune score (C), and tumor cellular purity (D). (E) KM survival analysis in the IMvigor210 cohort. (F–H) ESTIMATE algorithm outputs: immune score (F), ESTIMATE score (G), and tumor purity (H) between risk groups. (I) Disparities in risk ratings between the IMvigor210 cohort's CR/PR and SD/PD groups. (J) The histogram showed the TIDE score of each sample. (K) TIDE score by risk group. (L) Risk-TIDE score correlation. * $p < 0.05$, ** $p < 0.01$, *** $p < 0.001$, ns, no statistical significance.

First, qRT-PCR analysis of clinical samples confirmed that *CD40LG* mRNA expression was significantly down-regulated in OV tumor tissues versus normal controls ($p <$ 0.01; Fig. 6A). Next, KM survival analysis of the TCGA-OV cohort revealed significantly superior OS in patients with high *CD40LG* expression compared to those with low

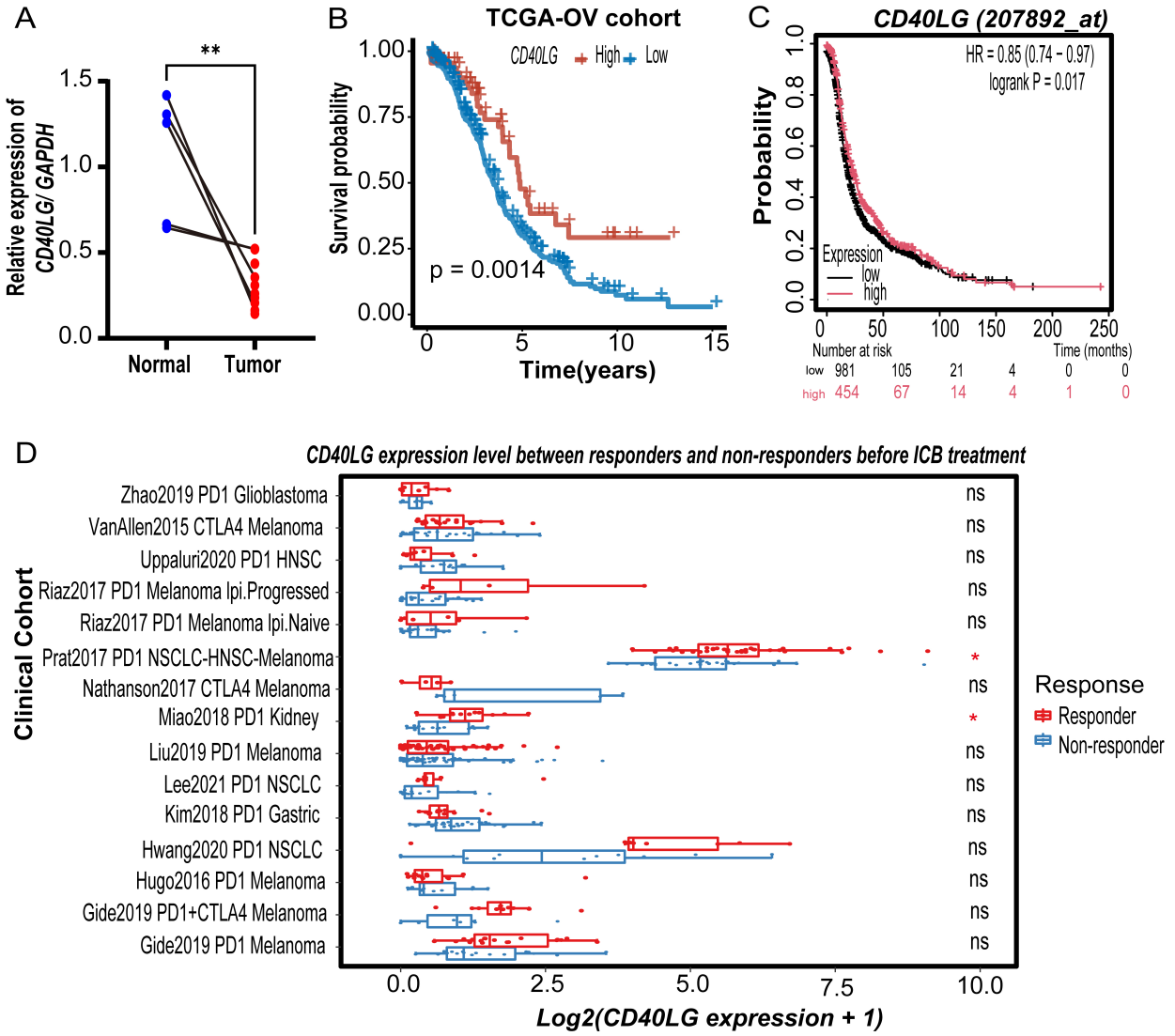

Fig. 6. Prognostic value, immunotherapeutic relevance, and cellular localization of *CD40LG* in ovarian cancer. (A) Quantification of *CD40LG* mRNA levels in OV versus normal ovarian specimens via qRT-PCR. (B) KM survival curve showing OS differences according to the tumor expression of *CD40LG*. (C) Independent validation of *CD40LG*'s prognostic value using the KM Plotter platform. (D) Comparison of *CD40LG* expression between ICB responders and non-responders. * $p < 0.05$, ** $p < 0.01$, ns, no statistical significance. qRT-PCR, quantitative real-time PCR.

CD40LG expression (Fig. 6B). This prognostic association was independently validated using the KM Plotter platform (https://kmplot.com/analysis/), which also showed that high *CD40LG* expression correlated with improved OS in a larger OV patient cohort (Fig. 6C).

To assess its relevance to immunotherapy, we analyzed data from immune checkpoint blockade (ICB) treatment cohorts using the ICRAFT platform (https://icraft.pku-genomics.org/#/homepage). Notably, *CD40LG* expression was significantly higher in ICB responders (CR/PR) compared to in non-responders (SD/PD) (Fig. 6D), suggesting that *CD40LG* may serve as a potential biomarker for predicting ICB sensitivity. Furthermore, integration of multiple single-cell RNA sequencing (scRNA-seq) datasets revealed that *CD40LG* was predominantly expressed in immune cells—specifically activated T cells and M1-polarized macrophages—rather than in malignant epithelial cells (Fig. 7). This cell-type-specific expression pattern aligns with *CD40LG*'s well-documented role as a T cell-derived co-stimulatory ligand that enhances anti-tumor immune responses, further supporting its potential as a therapeutic target within the tumor immune compartment.

Discussion

OV continues to be among the malignancies that pose the greatest clinical challenges, characterized by pronounced molecular heterogeneity and limited response to

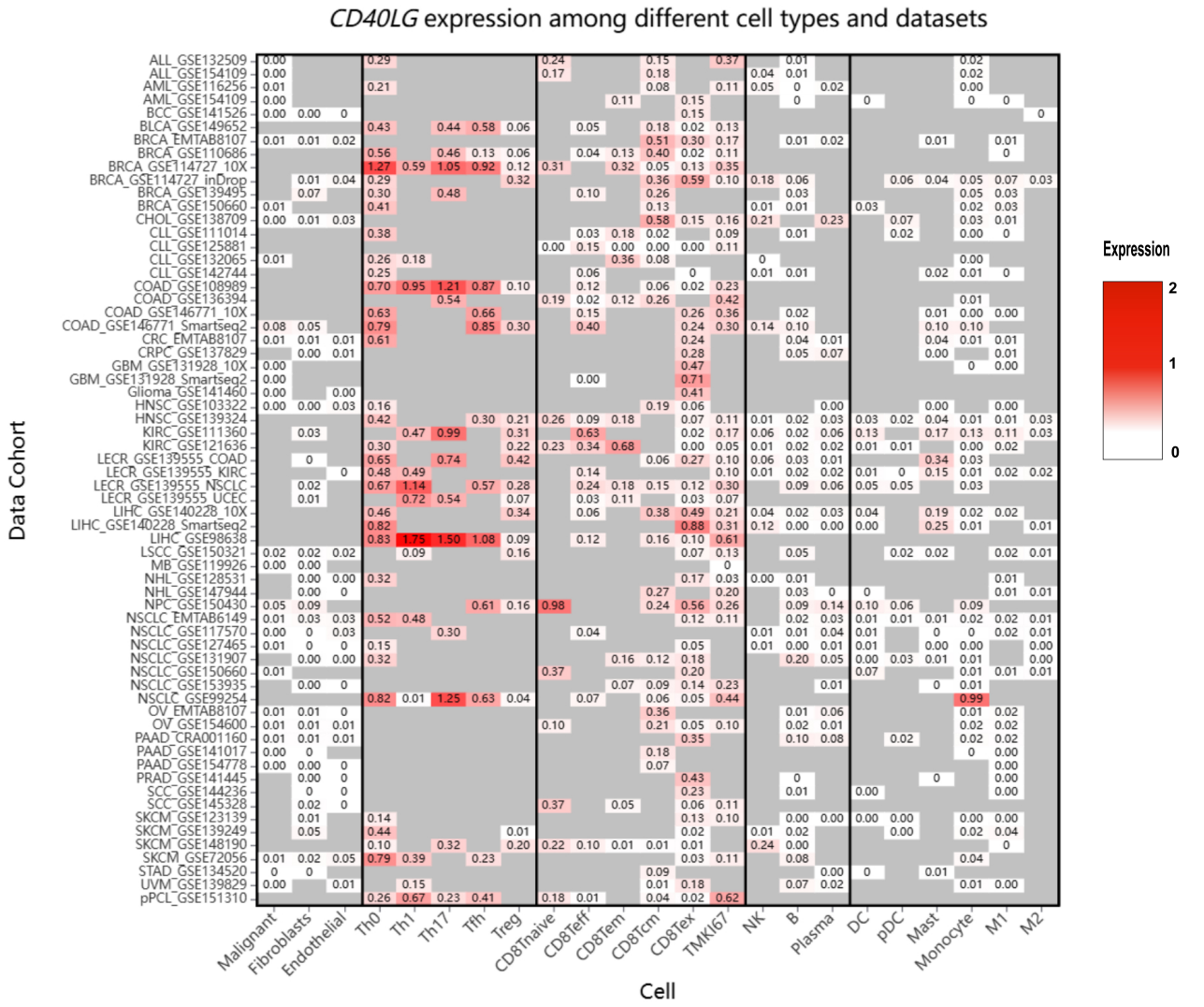

Fig. 7. *CD40LG*'s expression among different cell types and datasets. The color red indicates expression level, with darker red representing higher *CD40LG* expression levels.

immune checkpoint blockade (ICB), with durable clinical benefit observed in only a minority of patients [36–38]. While recent studies have identified immune checkpoint-related gene sets (e.g., *ICOS*, *TIGIT*, and *TNFRSF8*) for patient stratification based on co-expression with $CD8^+$ T cells [39], these approaches are limited by a narrow focus on canonical checkpoint biology, lack of integrated risk modeling, and absence of validation in ICB-treated cohorts. To address these limitations, we developed and validated a novel 6-gene IMPS for OV, integrating transcriptomic, clinical, and immunological data to dissect its biological basis and clinical utility, overcoming the scope constraints of previous models. The IMPS demonstrated robust discriminatory capability in the TCGA-OV training set, successfully stratifying the population into risk-defined subgroups with divergent OS outcomes. This was supported by 1-, 2-, 3-, and 5-year AUC values of 0.690, 0.720, 0.672, and 0.729, respectively, with the model's reliability further confirmed in the ICGC-OV external validation set. Notably, integration of clinical variables into a nomogram improved predictive performance (1-/3-/5-year AUCs: 0.719/0.714/0.731), yielding a clinically interpretable tool for risk-adapted decision-making.

The 6 genes comprising the IMPS (*HMGB3*, *IL27RA*, *BTLA*, *TNFRSF8*, *HLA-DOB*, and *CD40LG*) collectively regulate key immune-related circuits within the TME. As a DNA architectural protein with dual roles in maintaining genomic stability and regulating inflammation [40,41], *HMGB3* has been shown in pan-cancer analyses to be overexpressed in OV, where it acts as a favorable prognostic indicator and correlates positively with microsatellite instability and TMB [42]. This finding aligns with the TMB-integrated stratification capability of our IMPS to identify patients likely to benefit from immunotherapy. Paradoxically, *HMGB3* also promotes cancer stemness and platinum resistance through activation of the MAPK/ERK sig-

naling pathway [43]. This functional paradox may stem from TME heterogeneity, and its regulatory mechanisms require further investigation. *TNFRSF8* (*CD30*), which has been consistently associated with poor prognosis in OV [39], reinforces the IMPS's ability to capture the aggressive biological features of OV. In contrast, *BTLA*—an inhibitory checkpoint receptor that dampens T-cell responses via interaction with its ligand *HVEM* [44,45]—emerges as a possible therapeutic target and a predictive indicator. Preclinical studies have shown that *BTLA* blockade synergizes with chemotherapy to restore anti-tumor immune responses in OV models [46], supporting its translational value. Notably, *CD40LG*—a central co-stimulatory ligand in adaptive immunity—stands out as the most potent protective factor within the signature. Beyond its canonical role in dendritic cell maturation and T-cell priming [47–49], our study demonstrates three key findings: first, *CD40LG* is predominantly expressed in immune cells rather than tumor cells; second, its expression is significantly downregulated in OV tissues; and third, high *CD40LG* expression strongly correlates with improved OS. Critically, analysis of data from the ICRAFT platform revealed that *CD40LG* expression tended to be higher in ICB responders than in non-responders, positioning it as a promising target for *CD40* agonist-based therapies. This observation aligns with emerging clinical evidence that *CD40* activation can convert "cold" tumors—including pancreatic and biliary cancers—into immunoresponsive phenotypes, even in PD-1/PD-L1-resistant settings [50–52]. All of these results highlight the key role of the *CD40-CD40LG* axis in triggering anti-tumor immune response in OV and other solid tumors.

Functional and immunological profiling of the TCGA-OV cohort revealed marked biological differences between the high- and low-risk groups stratified by the IMPS. Specifically, the high-risk TME was characterized by enrichment of ECM-receptor interaction pathways, hyperactivation of MAPK signaling, and synergistic activation of the TGF-β/Wnt pathways—all processes well-documented to drive OV cell proliferation, epithelial-mesenchymal transition (EMT), and chemoresistance [53–56]. In contrast, the low-risk TME exhibited dominant enrichment of antigen processing/presentation and T-cell receptor signaling pathways—hallmarks of active adaptive anti-tumor immune activation [57–60]. This immunologically active phenotype in low-risk patients was further supported by increased infiltration of immune effector cells, including activated $CD4^+$ memory T cells, which provide T-cell help, and M1-polarized macrophages, which function as pro-inflammatory phagocytes [61,62].

Notably, the IMPS also demonstrated independent predictive value for ICB response, as validated in the IMvigor210 anti-PD-L1 cohort. Low-risk patients in this cohort exhibited significantly improved overall survival following anti-PD-L1 therapy, and risk scores were markedly lower in ICB responders (CR/PR) compared with non-responders (SD/PD). This observation aligns with the earlier finding that low-risk patients have lower TIDE scores (indicative of reduced immune evasion) and an immunologically active TME, both of which are features consistently linked to enhanced ICB efficacy in solid tumors [63,64]. While TMB correlated with improved OS in our cohort, consistent with its established role in boosting neoantigen-driven tumor immunogenicity [65,66], the correlation between TMB and risk score was weak ($r = -0.123$). Similarly, correlations between risk score and immune/ESTIMATE scores were modest. These statistically significant but weak correlations should be interpreted as supplementary biological context, rather than core evidence supporting the model's performance. The IMPS's primary strength lies in its robust prognostic stratification (validated by KM and ROC analyses) and its ability to predict ICB response, while the observed TME associations provide additional mechanistic insights.

However, several limitations should be considered, along with appropriate future initiatives. First, the IMPS was derived and validated using retrospective public cohorts (TCGA-OV, ICGC-OV) and a single external ICB trial (IMvigor210), which may result in selection bias and incomplete clinical annotation; prospective, multicenter validation in ethnically diverse OV patient populations is thus needed to confirm its generalizability. Second, while *CD40LG* was experimentally validated, the functional roles of the remaining five IMPS genes (*HMGB3*, *IL27RA*, *BTLA*, *TNFRSF8*, and *HLA-DOB*) and their regulatory crosstalk remain uncharacterized. Third, the IMPS-based nomogram, despite good prognostic performance, lacks prospective evidence to support its utility in guiding real-world treatment decisions. Fourth, validating the IMPS's association with TMB in broader independent datasets is an important direction for future research. To address these gaps, future research should prioritize elucidating the underlying mechanisms of *CD40-CD40LG* axis and other IMPS genes' functions in the OV TME, as well as conducting prospective trials to test the synergistic efficacy of *CD40* agonists plus PD-1/PD-L1 inhibitors, using the IMPS for patient stratification, which will advance the clinical translation of this combinatorial strategy, ultimately improving survival outcomes for OV patients.

Conclusions

In conclusion, our *CD40LG*-centered 6-gene prognostic signature provides a biologically grounded and clinically actionable framework for risk stratification and prediction of immunotherapy response in OV. At the core of this model, *CD40LG* functions as a consistent predictor of clinical outcomes and represents a potential site for therapeutic intervention—findings that open new avenues for exploring combinatorial immunotherapy strategies (e.g., *CD40*

agonists or adoptive T cell therapies). Notably, this signature provides practical support for guiding personalized immunotherapy selection, which aligns with the growing need for precision-based tools to assist in OV clinical decision-making.

Availability of Data and Materials

Publicly available datasets were analyzed in this study. These data can be found in the following repositories: RNA-seq data for ovarian cancer (n = 427) and normal tissues (n = 88) were sourced from the TCGA-TARGET-GTEx dataset on the UCSC Xena platform (https://xenabrowser.net/datapages/, accessed on January 17, 2024). Clinical metadata and RNA-seq data (TPM format) for the primary TCGA-OV cohort were downloaded from the GDC Data Portal (https://portal.gdc.cancer.gov/), Project ID: TCGA-OV. An independent validation cohort (OV-AU, n = 81) was acquired from the International Cancer Genome Consortium (ICGC) Data Portal (https://dcc.icgc.org), Project Code: OV-AU. Immunotherapy response data were obtained from the IMvigor210 cohort (http://research-pub.gene.com/IMvigor210CoreBiologies/).

Author Contributions

YG: Data curation, Methodology, writing—original draft preparation. MXY: Conceptualization, Formal Analysis, Resources, Supervision, Writing—review & editing. YWW: Data curation, Investigation, Visualization, Conceptualization, writing—original draft preparation. LW: Software, Data curation, Formal Analysis, Methodology, writing—original draft preparation. LAL: Investigation, Supervision, Project administration, Writing—review & editing. YGM: Conceptualization, Formal Analysis, Resources, Supervision, Validation, Visualization, Writing — review & editing. All authors have reviewed and approved the changes. All authors gave final approval of the version to be published. All authors have participated sufficiently in the work to take public responsibility for appropriate portions of the content and agreed to be accountable for all aspects of the work in ensuring that questions related to its accuracy or integrity.

Ethics Approval and Consent to Participate

This study was conducted in accordance with the Declaration of Helsinki, and ethical approval was obtained from the Ethics Committee of the Chinese PLA General Hospital (Approval No. of Ethics Committee: S2024-482-01). The participants provided their written informed consent to participate in this study.

Acknowledgment

We sincerely thank the public databases, including TCGA, UCSC, ICGC, KM plotter, and ICRAFT platform, for providing open access.

Funding

This research received no external funding.

Conflict of Interest

The authors declare no conflict of interest.

Supplementary Material

Supplementary material associated with this article can be found, in the online version, at https://doi.org/10.24976/Discov.Med.202638207.90.

References

[1] Smolarz B, Biernacka K, Łukasiewicz H, Samulak D, Piekarska E, Romanowicz H, *et al*. Ovarian Cancer-Epidemiology, Classification, Pathogenesis, Treatment, and Estrogen Receptors' Molecular Backgrounds. International Journal of Molecular Sciences. 2025; 26: 4611. https://doi.org/10.3390/ijms26104611.

[2] Sung H, Ferlay J, Siegel RL, Laversanne M, Soerjomataram I, Jemal A, *et al*. Global Cancer Statistics 2020: GLOBOCAN Estimates of Incidence and Mortality Worldwide for 36 Cancers in 185 Countries. CA: A Cancer Journal for Clinicians. 2021; 71: 209–249. https://doi.org/10.3322/caac.21660.

[3] Alizadeh H, Akbarabadi P, Dadfar A, Tareh MR, Soltani B. A comprehensive overview of ovarian cancer stem cells: correlation with high recurrence rate, underlying mechanisms, and therapeutic opportunities. Molecular Cancer. 2025; 24: 135. https://doi.org/10.1186/s12943-025-02345-3.

[4] Wang L, Zhang Q, Wang X, Dong Z, Liu S, Wang Q, *et al*. Therapeutic landscape of ovarian cancer: recent advances and emerging therapies. Biomarker Research. 2025; 13: 103. https://doi.org/10.1186/s40364-025-00818-7.

[5] Huo X, Tian T, Zhang X, Zhou N. Comparative effectiveness and safety of treatment regimens for recurrent advanced ovarian cancer: a systematic review and network meta-analysis. World Journal of Surgical Oncology. 2025; 23: 134. https://doi.org/10.1186/s12957-025-03770-w.

[6] Chen Z, Song Z, Den S, Zhang W, Han M, Lan T, *et al*. Application of Immune Checkpoint Inhibitors in Cancer. MedComm. 2025; 6: e70176. https://doi.org/10.1002/mco2.70176.

[7] Hinchcliff E, Hong D, Le H, Chisholm G, Iyer R, Naing A, *et al*. Characteristics and outcomes of patients with recurrent ovarian cancer undergoing early phase immune checkpoint inhibitor clinical trials. Gynecologic Oncology. 2018; 151: 407–413. https://doi.org/10.1016/j.ygyno.2018.10.008.

[8] Abiko K, Hamanishi J, Matsumura N, Mandai M. Dynamic host immunity and PD-L1/PD-1 blockade efficacy: developments after "IFN-γ from lymphocytes induces PD-L1 expression and promotes progression of ovarian cancer". British Journal of Cancer. 2023; 128: 461–467. https://doi.org/10.1038/s41416-022-01960-x.

[9] Arafat Hossain M. A comprehensive review of immune checkpoint inhibitors for cancer treatment. International Immunophar-

macology. 2024; 143: 113365. https://doi.org/10.1016/j.intimp.2024.113365.

[10] Weiss SA, Sznol M, Shaheen M, Berciano-Guerrero MÁ, Couselo EM, Rodríguez-Abreu D, *et al*. A Phase II Trial of the CD40 Agonistic Antibody Sotigalimab (APX005M) in Combination with Nivolumab in Subjects with Metastatic Melanoma with Confirmed Disease Progression on Anti-PD-1 Therapy. Clinical Cancer Research: an Official Journal of the American Association for Cancer Research. 2024; 30: 74–81. https://doi.org/10.1158/1078-0432.CCR-23-0475.

[11] Welsh RA, Sadegh-Nasseri S. The love and hate relationship of HLA-DM/DO in the selection of immunodominant epitopes. Current Opinion in Immunology. 2020; 64: 117–123. https://doi.org/10.1016/j.coi.2020.05.007.

[12] Sia TY, Manning-Geist B, Gordhandas S, Murali R, Marra A, Liu YL, *et al*. Treatment of ovarian clear cell carcinoma with immune checkpoint blockade: a case series. International Journal of Gynecological Cancer: Official Journal of the International Gynecological Cancer Society. 2022; 32: 1017–1024. https://doi.org/10.1136/ijgc-2022-003430.

[13] Joller N, Anderson AC, Kuchroo VK. LAG-3, TIM-3, and TIGIT: Distinct functions in immune regulation. Immunity. 2024; 57: 206–222. https://doi.org/10.1016/j.immuni.2024.01.010.

[14] Liang R, Ding D, Li Y, Lan T, Ryabtseva S, Huang S, *et al*. HDACi combination therapy with IDO1i remodels the tumor microenvironment and boosts antitumor efficacy in colorectal cancer with microsatellite stability. Journal of Nanobiotechnology. 2024; 22: 753. https://doi.org/10.1186/s12951-024-02936-0.

[15] Thapa B, Kato S, Nishizaki D, Miyashita H, Lee S, Nesline MK, *et al*. OX40/OX40 ligand and its role in precision immune oncology. Cancer Metastasis Reviews. 2024; 43: 1001–1013. https://doi.org/10.1007/s10555-024-10184-9.

[16] Goldman MJ, Craft B, Hastie M, Repečka K, McDade F, Kamath A, *et al*. Visualizing and interpreting cancer genomics data via the Xena platform. Nature Biotechnology. 2020; 38: 675–678. https://doi.org/10.1038/s41587-020-0546-8.

[17] Tian M, Yang J, Han J, He J, Liao W. A novel immune checkpoint-related seven-gene signature for predicting prognosis and immunotherapy response in melanoma. International Immunopharmacology. 2020; 87: 106821. https://doi.org/10.1016/j.intimp.2020.106821.

[18] Hu FF, Liu CJ, Liu LL, Zhang Q, Guo AY. Expression profile of immune checkpoint genes and their roles in predicting immunotherapy response. Briefings in Bioinformatics. 2021; 22: bbaa176. https://doi.org/10.1093/bib/bbaa176.

[19] Xu D, Liu X, Wang Y, Zhou K, Wu J, Chen JC, *et al*. Identification of immune subtypes and prognosis of hepatocellular carcinoma based on immune checkpoint gene expression profile. Biomedicine & Pharmacotherapy = Biomedecine & Pharmacotherapie. 2020; 126: 109903. https://doi.org/10.1016/j.biopha.2020.109903.

[20] Yu Y, Tang H, Franceschi D, Mujagond P, Acharya A, Deng Y, *et al*. Immune Checkpoint Gene Expression Profiling Identifies Programmed Cell Death Ligand-1 Centered Immunologic Subtypes of Oral and Squamous Cell Carcinoma With Favorable Survival. Frontiers in Medicine. 2022; 8: 759605. https://doi.org/10.3389/fmed.2021.759605.

[21] Guo Y, Bao J, Lin D, Hong K, Cen K, Sun J, *et al*. Novel immune checkpoint-related gene model to predict prognosis and treatment responsiveness in low-grade gliomas. Heliyon. 2023; 9: e20178. https://doi.org/10.1016/j.heliyon.2023.e20178.

[22] Jain R, Xu W. HDSI: High dimensional selection with interactions algorithm on feature selection and testing. PloS One. 2021; 16: e0246159. https://doi.org/10.1371/journal.pone.0246159.

[23] Wu T, Hu E, Xu S, Chen M, Guo P, Dai Z, *et al*. clusterProfiler 4.0: A universal enrichment tool for interpreting omics data. Innovation (Cambridge (Mass.)). 2021; 2: 100141. https://doi.org/10.1016/j.xinn.2021.100141.

[24] Huang Y, Wang X, Cao Y, Lan X, Hu X, Mou F, *et al*. Nomogram for Predicting Neoadjuvant Chemotherapy Response in Breast Cancer Using MRI-based Intratumoral Heterogeneity Quantification. Radiology. 2025; 315: e241805. https://doi.org/10.1148/radiol.241805.

[25] Balachandran VP, Gonen M, Smith JJ, DeMatteo RP. Nomograms in oncology: more than meets the eye. The Lancet. Oncology. 2015; 16: e173–e180. https://doi.org/10.1016/S1470-2045(14)71116-7.

[26] Cerami E, Gao J, Dogrusoz U, Gross BE, Sumer SO, Aksoy BA, *et al*. The cBio cancer genomics portal: an open platform for exploring multidimensional cancer genomics data. Cancer Discovery. 2012; 2: 401–404. https://doi.org/10.1158/2159-8290.CD-12-0095.

[27] Sinha N, Sinha S, Valero C, Schäffer AA, Aldape K, Litchfield K, *et al*. Immune Determinants of the Association between Tumor Mutational Burden and Immunotherapy Response across Cancer Types. Cancer Research. 2022; 82: 2076–2083. https://doi.org/10.1158/0008-5472.CAN-21-2542.

[28] Zeng D, Ye Z, Shen R, Yu G, Wu J, Xiong Y, *et al*. IOBR: Multi-Omics Immuno-Oncology Biological Research to Decode Tumor Microenvironment and Signatures. Frontiers in Immunology. 2021; 12: 687975. https://doi.org/10.3389/fimmu.2021.687975.

[29] Yoshihara K, Shahmoradgoli M, Martínez E, Vegesna R, Kim H, Torres-Garcia W, *et al*. Inferring tumour purity and stromal and immune cell admixture from expression data. Nature Communications. 2013; 4: 2612. https://doi.org/10.1038/ncomms3612.

[30] Li Y, Pan X, Luo W, Gamalla Y, Ma Z, Zhou P, *et al*. TMErisk score: A tumor microenvironment-based model for predicting prognosis and immunotherapy in patients with head and neck squamous cell carcinoma. Heliyon. 2024; 10: e31877. https://doi.org/10.1016/j.heliyon.2024.e31877.

[31] Jiang P, Gu S, Pan D, Fu J, Sahu A, Hu X, *et al*. Signatures of T cell dysfunction and exclusion predict cancer immunotherapy response. Nature Medicine. 2018; 24: 1550–1558. https://doi.org/10.1038/s41591-018-0136-1.

[32] Li J, Wang N, Mao G, Wang J, Xiang M, Zhang H, *et al*. Cuproptosis-associated lncRNA impact prognosis in patients with non-small cell lung cancer co-infected with COVID-19. Journal of Cellular and Molecular Medicine. 2024; 28: e70059. https://doi.org/10.1111/jcmm.70059.

[33] Pérez-Guijarro E, Yang HH, Araya RE, El Meskini R, Michael HT, Vodnala SK, *et al*. Multimodel preclinical platform predicts clinical response of melanoma to immunotherapy. Nature Medicine. 2020; 26: 781–791. https://doi.org/10.1038/s41591-020-0818-3.

[34] Mihaila RI, Gheorghe AS, Zob DL, Stanculeanu DL. The Importance of Predictive Biomarkers and Their Correlation with the Response to Immunotherapy in Solid Tumors-Impact on Clinical Practice. Biomedicines. 2024; 12: 2146. https://doi.org/10.3390/biomedicines12092146.

[35] Wu B, Zhang B, Li B, Wu H, Jiang M. Cold and hot tumors: from molecular mechanisms to targeted therapy. Signal Transduction and Targeted Therapy. 2024; 9: 274. https://doi.org/10.1038/s41392-024-01979-x.

[36] Lheureux S, Braunstein M, Oza AM. Epithelial ovarian cancer: Evolution of management in the era of precision medicine. CA: A Cancer Journal for Clinicians. 2019; 69: 280–304. https://doi.org/10.3322/caac.21559.

[37] Konstantinopoulos PA, Matulonis UA. Clinical and translational advances in ovarian cancer therapy. Nature Cancer. 2023; 4:

1239–1257. https://doi.org/10.1038/s43018-023-00617-9.

[38] Ghisoni E, Morotti M, Sarivalasis A, Grimm AJ, Kandalaft L, Laniti DD, *et al*. Immunotherapy for ovarian cancer: towards a tailored immunophenotype-based approach. Nature Reviews. Clinical Oncology. 2024; 21: 801–817. https://doi.org/10.1038/s41571-024-00937-4.

[39] Huo X, Zhang X, Li S, Wang S, Sun H, Yang M. Identification of Novel Immunologic Checkpoint Gene Prognostic Markers for Ovarian Cancer. Journal of Oncology. 2022; 2022: 8570882. https://doi.org/10.1155/2022/8570882.

[40] Wang L, Xu P, Li X, Zhang Q. Comprehensive bioinformatics analysis identified HMGB3 as a promising immunotherapy target for glioblastoma multiforme. Discover Oncology. 2025; 16: 478. https://doi.org/10.1007/s12672-025-02235-6.

[41] Chikhirzhina E, Tsimokha A, Tomilin AN, Polyanichko A. Structure and Functions of HMGB3 Protein. International Journal of Molecular Sciences. 2024; 25: 7656. https://doi.org/10.3390/ijms25147656.

[42] Lin T, Zhang Y, Lin Z, Peng L. Roles of HMGBs in Prognosis and Immunotherapy: A Pan-Cancer Analysis. Frontiers in Genetics. 2021; 12: 764245. https://doi.org/10.3389/fgene.2021.764245.

[43] Ma H, Qi G, Han F, Gai P, Peng J, Kong B. HMGB3 promotes the malignant phenotypes and stemness of epithelial ovarian cancer through the MAPK/ERK signaling pathway. Cell Communication and Signaling: CCS. 2023; 21: 144. https://doi.org/10.1186/s12964-023-01172-7.

[44] Andrzejczak A, Karabon L. BTLA biology in cancer: from bench discoveries to clinical potentials. Biomarker Research. 2024; 12: 8. https://doi.org/10.1186/s40364-024-00556-2.

[45] Wojciechowicz K, Spodzieja M, Wardowska A. The BTLA-HVEM complex - The future of cancer immunotherapy. European Journal of Medicinal Chemistry. 2024; 268: 116231. https://doi.org/10.1016/j.ejmech.2024.116231.

[46] Chen YL, Lin HW, Chien CL, Lai YL, Sun WZ, Chen CA, *et al*. BTLA blockade enhances Cancer therapy by inhibiting IL-6/IL-10-induced $CD19^{high}$ B lymphocytes. Journal for Immunotherapy of Cancer. 2019; 7: 313. https://doi.org/10.1186/s40425-019-0744-4.

[47] Tang T, Cheng X, Truong B, Sun L, Yang X, Wang H. Molecular basis and therapeutic implications of CD40/CD40L immune checkpoint. Pharmacology & Therapeutics. 2021; 219: 107709. https://doi.org/10.1016/j.pharmthera.2020.107709.

[48] Melichar B, Patenia R, Gallardo S, Melicharová K, Hu W, Freedman RS. Expression of CD40 and growth-inhibitory activity of CD40 ligand in ovarian cancer cell lines. Gynecologic Oncology. 2007; 104: 707–713. https://doi.org/10.1016/j.ygyno.2006.10.056.

[49] Ghamande S, Hylander BL, Oflazoglu E, Lele S, Fanslow W, Repasky EA. Recombinant CD40 ligand therapy has significant antitumor effects on CD40-positive ovarian tumor xenografts grown in SCID mice and demonstrates an augmented effect with cisplatin. Cancer Research. 2001; 61: 7556–7562.

[50] Vonderheide RH. CD40 Agonist Antibodies in Cancer Immunotherapy. Annual Review of Medicine. 2020; 71: 47–58. https://doi.org/10.1146/annurev-med-062518-045435.

[51] Diggs LP, Ruf B, Ma C, Heinrich B, Cui L, Zhang Q, *et al*. CD40-mediated immune cell activation enhances response to anti-PD-1 in murine intrahepatic cholangiocarcinoma. Journal of Hepatology. 2021; 74: 1145–1154. https://doi.org/10.1016/j.jhep.2020.11.037.

[52] Morrison AH, Diamond MS, Hay CA, Byrne KT, Vonderheide RH. Sufficiency of CD40 activation and immune checkpoint blockade for T cell priming and tumor immunity. Proceedings of the National Academy of Sciences of the United States of America. 2020; 117: 8022–8031. https://doi.org/10.1073/pnas.1918971117.

[53] Yan L, Song Z, Yi L, Tian C, Zhang R, Qin X, *et al*. TMEM176B inhibits ovarian cancer progression by regulating EMT via the Wnt/β-catenin signaling pathway. Journal of Translational Medicine. 2025; 23: 350. https://doi.org/10.1186/s12967-025-06362-0.

[54] Wang X, Eichhorn PJA, Thiery JP. TGF-β, EMT, and resistance to anti-cancer treatment. Seminars in Cancer Biology. 2023; 97: 1–11. https://doi.org/10.1016/j.semcancer.2023.10.004.

[55] Bahar ME, Kim HJ, Kim DR. Targeting the RAS/RAF/MAPK pathway for cancer therapy: from mechanism to clinical studies. Signal Transduction and Targeted Therapy. 2023; 8: 455. https://doi.org/10.1038/s41392-023-01705-z.

[56] Brown Y, Hua S, Tanwar PS. Extracellular matrix in high-grade serous ovarian cancer: Advances in understanding of carcinogenesis and cancer biology. Matrix Biology: Journal of the International Society for Matrix Biology. 2023; 118: 16–46. https://doi.org/10.1016/j.matbio.2023.02.004.

[57] Zhang Y, Zhang Z. The history and advances in cancer immunotherapy: understanding the characteristics of tumor-infiltrating immune cells and their therapeutic implications. Cellular & Molecular Immunology. 2020; 17: 807–821. https://doi.org/10.1038/s41423-020-0488-6.

[58] Chap BS, Rayroux N, Grimm AJ, Ghisoni E, Dangaj Laniti D. Crosstalk of T cells within the ovarian cancer microenvironment. Trends in Cancer. 2024; 10: 1116–1130. https://doi.org/10.1016/j.trecan.2024.09.001.

[59] Jhunjhunwala S, Hammer C, Delamarre L. Antigen presentation in cancer: insights into tumour immunogenicity and immune evasion. Nature Reviews. Cancer. 2021; 21: 298–312. https://doi.org/10.1038/s41568-021-00339-z.

[60] Peng S, Yan Y, Ogino K, Ma G, Xia Y. Spatiotemporal coordination of antigen presentation and co-stimulatory signal for enhanced anti-tumor vaccination. Journal of Controlled Release: Official Journal of the Controlled Release Society. 2024; 374: 312–324. https://doi.org/10.1016/j.jconrel.2024.08.025.

[61] Zhang W, Wang M, Ji C, Liu X, Gu B, Dong T. Macrophage polarization in the tumor microenvironment: Emerging roles and therapeutic potentials. Biomedicine & Pharmacotherapy = Biomedecine & Pharmacotherapie. 2024; 177: 116930. https://doi.org/10.1016/j.biopha.2024.116930.

[62] Franken A, Bila M, Mechels A, Kint S, Van Dessel J, Pomella V, *et al*. $CD4^+$ T cell activation distinguishes response to anti-PD-L1+anti-CTLA4 therapy from anti-PD-L1 monotherapy. Immunity. 2024; 57: 541–558.e7. https://doi.org/10.1016/j.immuni.2024.02.007.

[63] Blanc-Durand F, Clemence Wei Xian L, Tan DSP. Targeting the immune microenvironment for ovarian cancer therapy. Frontiers in Immunology. 2023; 14: 1328651. https://doi.org/10.3389/fimmu.2023.1328651.

[64] Kumagai S, Itahashi K, Nishikawa H. Regulatory T cell-mediated immunosuppression orchestrated by cancer: towards an immuno-genomic paradigm for precision medicine. Nature Reviews. Clinical Oncology. 2024; 21: 337–353. https://doi.org/10.1038/s41571-024-00870-6.

[65] Jardim DL, Goodman A, de Melo Gagliato D, Kurzrock R. The Challenges of Tumor Mutational Burden as an Immunotherapy Biomarker. Cancer Cell. 2021; 39: 154–173. https://doi.org/10.1016/j.ccell.2020.10.001.

[66] Zheng M. Super-high tumor mutational burden predicts complete remission following immunotherapy: from Peto's paradox to druggable cancer hallmark. Journal for Immunotherapy of Cancer. 2025; 13: e010486. https://doi.org/10.1136/jitc-2024-010486.